Centrality dependence of identified particle elliptic flow in relativistic heavy ion collisions at √sNN = 7.7–62.4 GeV

(STAR Collaboration) Adamczyk, L.; ...; Planinić, Mirko; ...; Poljak, Nikola; ...; Zyzak, M.

Source / Izvornik: **Physical Review C, 2016, 93**

Journal article, Published version
Rad u časopisu, Objavljena verzija rada (izdavačev PDF)

https://doi.org/10.1103/PhysRevC.93.014907

Permanent link / Trajna poveznica: https://urn.nsk.hr/urn:nbn:hr:217:811525

Centrality dependence of identified particle elliptic flow in relativistic heavy ion collisions at $\sqrt{s_{NN}} = 7.7$–62.4 GeV

L. Adamczyk,[1] J. K. Adkins,[20] G. Agakishiev,[18] M. M. Aggarwal,[30] Z. Ahammed,[48] I. Alekseev,[16] A. Aparin,[18] D. Arkhipkin,[3] E. C. Aschenauer,[3] G. S. Averichev,[18] X. Bai,[8] V. Bairathi,[27] A. Banerjee,[48] R. Bellwied,[44] A. Bhasin,[17] A. K. Bhati,[30] P. Bhattarai,[43] J. Bielcik,[10] J. Bielcikova,[11] L. C. Bland,[3] I. G. Bordyuzhin,[16] J. Bouchet,[19] D. Brandenburg,[36] A. V. Brandin,[26] I. Bunzarov,[18] J. Butterworth,[36] H. Caines,[52] M. Calderón de la Barca Sánchez,[5] J. M. Campbell,[28] D. Cebra,[5] M. C. Cervantes,[42] I. Chakaberia,[3] P. Chaloupka,[10] Z. Chang,[42] S. Chattopadhyay,[48] X. Chen,[22] J. H. Chen,[39] J. Cheng,[45] M. Cherney,[9] O. Chisman,[6] W. Christie,[3] G. Contin,[23] H. J. Crawford,[4] S. Das,[13] L. C. De Silva,[9] R. R. Debbe,[3] T. G. Dedovich,[18] J. Deng,[38] A. A. Derevschikov,[32] B. di Ruzza,[3] L. Didenko,[3] C. Dilks,[31] X. Dong,[23] J. L. Drachenberg,[47] J. E. Draper,[5] C. M. Du,[22] L. E. Dunkelberger,[6] J. C. Dunlop,[3] L. G. Efimov,[18] J. Engelage,[4] G. Eppley,[36] R. Esha,[6] O. Evdokimov,[8] O. Eyser,[3] R. Fatemi,[20] S. Fazio,[3] P. Federic,[11] J. Fedorisin,[18] Z. Feng,[7] P. Filip,[18] Y. Fisyak,[3] C. E. Flores,[5] L. Fulek,[1] C. A. Gagliardi,[42] D. Garand,[33] F. Geurts,[36] A. Gibson,[47] M. Girard,[49] L. Greiner,[23] D. Grosnick,[47] D. S. Gunarathne,[41] Y. Guo,[37] A. Gupta,[17] S. Gupta,[17] W. Guryn,[3] A. Hamad,[19] A. Hamed,[42] R. Haque,[27] J. W. Harris,[52] L. He,[33] S. Heppelmann,[3] S. Heppelmann,[31] A. Hirsch,[33] G. W. Hoffmann,[43] D. J. Hofman,[8] S. Horvat,[52] H. Z. Huang,[6] B. Huang,[8] X. Huang,[45] P. Huck,[7] T. J. Humanic,[28] G. Igo,[6] W. W. Jacobs,[15] H. Jang,[21] K. Jiang,[37] E. G. Judd,[4] S. Kabana,[19] D. Kalinkin,[16] K. Kang,[45] K. Kauder,[50] H. W. Ke,[3] D. Keane,[19] A. Kechechyan,[18] Z. H. Khan,[8] D. P. Kikoła,[49] I. Kisel,[12] A. Kisiel,[49] L. Kochenda,[26] D. D. Koetke,[47] T. Kollegger,[12] L. K. Kosarzewski,[49] A. F. Kraishan,[41] P. Kravtsov,[26] K. Krueger,[2] I. Kulakov,[12] L. Kumar,[30] R. A. Kycia,[29] M. A. C. Lamont,[3] J. M. Landgraf,[3] K. D. Landry,[6] J. Lauret,[3] A. Lebedev,[3] R. Lednicky,[18] J. H. Lee,[3] X. Li,[41] Y. Li,[45] W. Li,[39] C. Li,[37] X. Li,[3] Z. M. Li,[7] M. A. Lisa,[28] F. Liu,[7] T. Ljubicic,[3] W. J. Llope,[50] M. Lomnitz,[19] R. S. Longacre,[3] X. Luo,[7] L. Ma,[39] Y. G. Ma,[39] G. L. Ma,[39] R. Ma,[3] N. Magdy,[40] R. Majka,[52] A. Manion,[23] S. Margetis,[19] C. Markert,[43] H. Masui,[23] H. S. Matis,[23] D. McDonald,[44] K. Meehan,[5] N. G. Minaev,[32] S. Mioduszewski,[42] D. Mishra,[27] B. Mohanty,[27] M. M. Mondal,[42] D. A. Morozov,[32] M. K. Mustafa,[23] B. K. Nandi,[14] Md. Nasim,[6] T. K. Nayak,[48] G. Nigmatkulov,[26] T. Niida,[50] L. V. Nogach,[32] S. Y. Noh,[21] J. Novak,[25] S. B. Nurushev,[32] G. Odyniec,[23] A. Ogawa,[3] K. Oh,[34] V. Okorokov,[26] D. Olvitt Jr.,[41] B. S. Page,[3] R. Pak,[3] Y. X. Pan,[6] Y. Pandit,[8] Y. Panebratsev,[18] B. Pawlik,[29] H. Pei,[7] C. Perkins,[4] A. Peterson,[28] P. Pile,[3] M. Planinic,[53] J. Pluta,[49] N. Poljak,[53] K. Poniatowska,[49] J. Porter,[23] M. Posik,[41] A. M. Poskanzer,[23] N. K. Pruthi,[30] J. Putschke,[50] H. Qiu,[23] A. Quintero,[19] S. Ramachandran,[20] S. Raniwala,[35] R. Raniwala,[35] R. L. Ray,[43] H. G. Ritter,[23] J. B. Roberts,[36] O. V. Rogachevskiy,[18] J. L. Romero,[5] A. Roy,[48] L. Ruan,[3] J. Rusnak,[11] O. Rusnakova,[10] N. R. Sahoo,[42] P. K. Sahu,[13] S. Salur,[23] J. Sandweiss,[52] A. Sarkar,[14] J. Schambach,[43] R. P. Scharenberg,[33] A. M. Schmah,[23] W. B. Schmidke,[3] N. Schmitz,[24] J. Seger,[9] P. Seyboth,[24] N. Shah,[39] E. Shahaliev,[18] P. V. Shanmuganathan,[19] M. Shao,[37] B. Sharma,[30] M. K. Sharma,[17] W. Q. Shen,[39] S. S. Shi,[7] Q. Y. Shou,[39] E. P. Sichtermann,[23] R. Sikora,[1] M. Simko,[11] S. Singha,[19] M. J. Skoby,[15] N. Smirnov,[52] D. Smirnov,[3] L. Song,[44] P. Sorensen,[3] H. M. Spinka,[2] B. Srivastava,[33] T. D. S. Stanislaus,[47] M. Stepanov,[33] R. Stock,[12] M. Strikhanov,[26] B. Stringfellow,[33] M. Sumbera,[11] B. Summa,[31] X. Sun,[23] Z. Sun,[22] Y. Sun,[37] X. M. Sun,[7] B. Surrow,[41] N. Svirida,[16] M. A. Szelezniak,[23] Z. Tang,[37] A. H. Tang,[3] T. Tarnowsky,[25] A. Tawfik,[51] J. Thäder,[23] J. H. Thomas,[23] A. R. Timmins,[44] D. Tlusty,[11] M. Tokarev,[18] S. Trentalange,[6] R. E. Tribble,[42] P. Tribedy,[3] S. K. Tripathy,[13] B. A. Trzeciak,[10] O. D. Tsai,[6] T. Ullrich,[3] D. G. Underwood,[2] I. Upsal,[28] G. Van Buren,[3] G. van Nieuwenhuizen,[3] M. Vandenbroucke,[41] R. Varma,[14] A. N. Vasiliev,[32] R. Vertesi,[11] F. Videbæk,[3] Y. P. Viyogi,[48] S. Vokal,[18] S. A. Voloshin,[50] A. Vossen,[15] F. Wang,[33] Y. Wang,[45] G. Wang,[6] Y. Wang,[7] J. S. Wang,[22] H. Wang,[3] J. C. Webb,[3] G. Webb,[3] L. Wen,[6] G. D. Westfall,[25] H. Wieman,[23] S. W. Wissink,[15] R. Witt,[46] Y. F. Wu,[7] Y. Wu,[19] Z. G. Xiao,[45] W. Xie,[33] K. Xin,[36] Z. Xu,[3] H. Xu,[22] Y. F. Xu,[39] Q. H. Xu,[38] N. Xu,[23] Y. Yang,[22] C. Yang,[37] S. Yang,[37] Y. Yang,[7] Q. Yang,[37] Z. Ye,[8] Z. Ye,[8] P. Yepes,[36] L. Yi,[52] K. Yip,[3] I.-K. Yoo,[34] N. Yu,[7] H. Zbroszczyk,[49] W. Zha,[37] J. B. Zhang,[7] Y. Zhang,[37] S. Zhang,[39] J. Zhang,[38] J. Zhang,[22] Z. Zhang,[39] X. P. Zhang,[45] J. Zhao,[7] C. Zhong,[39] L. Zhou,[37] X. Zhu,[45] Y. Zoulkarneeva,[18] and M. Zyzak[12]

(STAR Collaboration)

[1]*AGH University of Science and Technology, Cracow 30-059, Poland*

[2]*Argonne National Laboratory, Argonne, Illinois 60439, USA*

[3]*Brookhaven National Laboratory, Upton, New York 11973, USA*

[4]*University of California, Berkeley, California 94720, USA*

[5]*University of California, Davis, California 95616, USA*

[6]*University of California, Los Angeles, California 90095, USA*

[7]*Central China Normal University (HZNU), Wuhan 430079, China*

[8]*University of Illinois at Chicago, Chicago, Illinois 60607, USA*

[9]*Creighton University, Omaha, Nebraska 68178, USA*

[10]*Czech Technical University in Prague, FNSPE, Prague, 115 19, Czech Republic*

[11]*Nuclear Physics Institute AS CR, 250 68 Řež/Prague, Czech Republic*

[12]*Frankfurt Institute for Advanced Studies FIAS, Frankfurt 60438, Germany*

[13]*Institute of Physics, Bhubaneswar 751005, India*

[14]*Indian Institute of Technology, Mumbai 400076, India*

[15]*Indiana University, Bloomington, Indiana 47408, USA*

[16]*Alikhanov Institute for Theoretical and Experimental Physics, Moscow 117218, Russia*
[17]*University of Jammu, Jammu 180001, India*
[18]*Joint Institute for Nuclear Research, Dubna, 141 980, Russia*
[19]*Kent State University, Kent, Ohio 44242, USA*
[20]*University of Kentucky, Lexington, Kentucky, 40506-0055, USA*
[21]*Korea Institute of Science and Technology Information, Daejeon 305-701, Korea*
[22]*Institute of Modern Physics, Lanzhou 730000, China*
[23]*Lawrence Berkeley National Laboratory, Berkeley, California 94720, USA*
[24]*Max-Planck-Institut fur Physik, Munich 80805, Germany*
[25]*Michigan State University, East Lansing, Michigan 48824, USA*
[26]*Moscow Engineering Physics Institute, Moscow 115409, Russia*
[27]*National Institute of Science Education and Research, Bhubaneswar 751005, India*
[28]*Ohio State University, Columbus, Ohio 43210, USA*
[29]*Institute of Nuclear Physics PAN, Cracow 31-342, Poland*
[30]*Panjab University, Chandigarh 160014, India*
[31]*Pennsylvania State University, University Park, Pennsylvania 16802, USA*
[32]*Institute of High Energy Physics, Protvino 142281, Russia*
[33]*Purdue University, West Lafayette, Indiana 47907, USA*
[34]*Pusan National University, Pusan 609735, Republic of Korea*
[35]*University of Rajasthan, Jaipur 302004, India*
[36]*Rice University, Houston, Texas 77251, USA*
[37]*University of Science and Technology of China, Hefei 230026, China*
[38]*Shandong University, Jinan, Shandong 250100, China*
[39]*Shanghai Institute of Applied Physics, Shanghai 201800, China*
[40]*State University Of New York, Stony Brook, New York 11794, USA*
[41]*Temple University, Philadelphia, Pennsylvania 19122, USA*
[42]*Texas A&M University, College Station, Texas 77843, USA*
[43]*University of Texas, Austin, Texas 78712, USA*
[44]*University of Houston, Houston, Texas 77204, USA*
[45]*Tsinghua University, Beijing 100084, China*
[46]*United States Naval Academy, Annapolis, Maryland, 21402, USA*
[47]*Valparaiso University, Valparaiso, Indiana 46383, USA*
[48]*Variable Energy Cyclotron Centre, Kolkata 700064, India*
[49]*Warsaw University of Technology, Warsaw 00-661, Poland*
[50]*Wayne State University, Detroit, Michigan 48201, USA*
[51]*World Laboratory for Cosmology and Particle Physics (WLCAPP), Cairo 11571, Egypt*
[52]*Yale University, New Haven, Connecticut 06520, USA*
[53]*University of Zagreb, Zagreb, HR-10002, Croatia*

(Received 29 September 2015; published 19 January 2016)

Elliptic flow (v_2) values for identified particles at midrapidity in Au + Au collisions measured by the STAR experiment in the Beam Energy Scan at the Relativistic Heavy Ion Collider at $\sqrt{s_{NN}} = 7.7$–62.4 GeV are presented for three centrality classes. The centrality dependence and the data at $\sqrt{s_{NN}} = 14.5$ GeV are new. Except at the lowest beam energies, we observe a similar relative v_2 baryon-meson splitting for all centrality classes which is in agreement within 15% with the number-of-constituent quark scaling. The larger v_2 for most particles relative to antiparticles, already observed for minimum bias collisions, shows a clear centrality dependence, with the largest difference for the most central collisions. Also, the results are compared with a multiphase transport (AMPT) model and fit with a blast wave model.

DOI: 10.1103/PhysRevC.93.014907

I. INTRODUCTION

The Beam Energy Scan (BES) program at the Relativistic Heavy Ion Collider (RHIC) facility was initiated in the year 2010 to study the quantum chromodynamics (QCD) phase diagram [1]. In the years 2010 and 2011 the STAR (Solenoidal Tracker at RHIC) experiment recorded Au + Au collisions at $\sqrt{s_{NN}} = 7.7$, 11.5, 19.6, 27, 39, and 62.4 GeV. In the year 2014 data were recorded at 14.5 GeV. The results reported here are for a pseudorapidity range of $|\eta| < 1$. Recently published results from identified particle elliptic flow (v_2) in minimum bias (0%–80% centrality) collisions revealed an energy-dependent difference in elliptic flow between particles and

antiparticles [2]. This difference is increasing with decreasing collision energy and is almost identical for all baryons. It is larger for baryons than mesons. These observations attracted the attention of various theory groups, which tried to reproduce the results with different assumptions in their model calculations. (See Refs. [25–28] in Ref. [2].) The most recent attempts are found in Ref. [3], which uses three-fluid dynamics, and Ref. [4], which keeps the equilibration but varies the chemical potential. In this paper we present the energy and centrality dependence of identified particle elliptic flow. The new centrality dependence might be important for distinguishing between the different models or for improving their input parameters.

This paper is organized as follows. Section II presents the recent minimum bias data at $\sqrt{s_{NN}} = 14.5$ GeV. Section III presents the centrality and energy dependence of v_2 as a function of transverse kinetic energy $m_T - m_0$. Section IV shows a comparison with a multiphase transport (AMPT) model calculation. In Sec. V, blast wave fits to the data are shown and the results for the transverse expansion velocity as a function of beam energy are discussed. A summary is presented in Sec. VI.

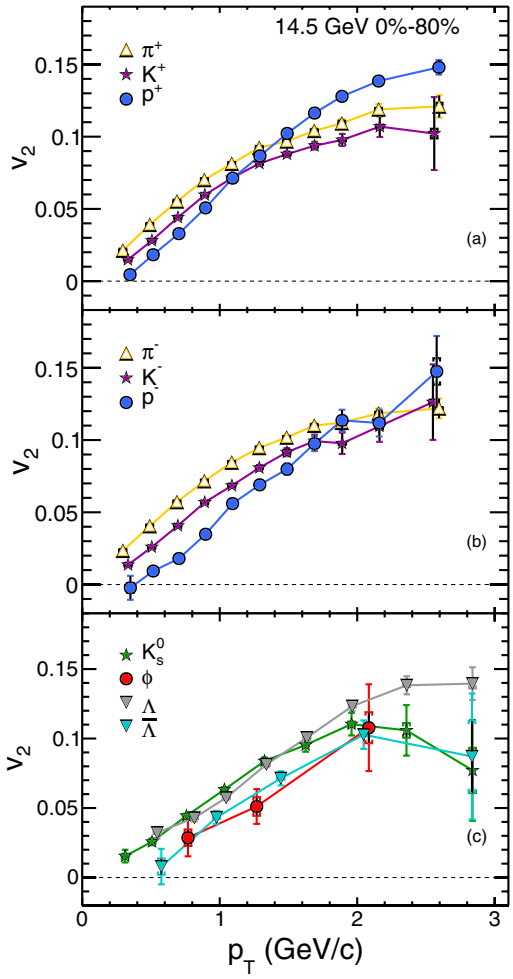

FIG. 1. Elliptic flow v_2 as a function of p_T for minimum bias data (0%–80% centrality) at $\sqrt{s_{NN}} = 14.5$ GeV for identified particles. (a) Positively charged particles. (b) Negatively charged particles. (c) Neutral particles. The systematic errors are shown by the short error bars with caps. The lines connect the points.

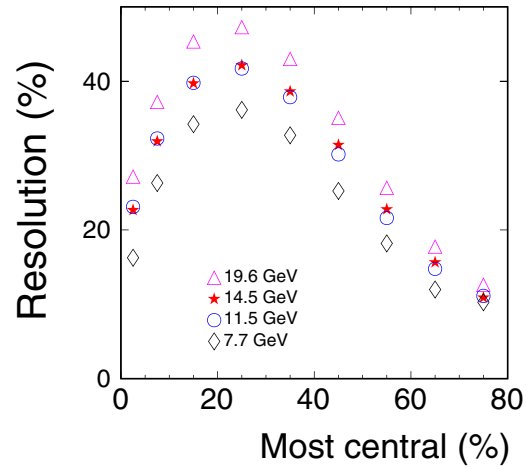

FIG. 2. The subevent plane resolution for several beam energies versus centrality with 5% being the most central.

II. 14.5 GeV DATA

The data obtained in 2014 at $\sqrt{s_{NN}} = 14.5$ GeV were analyzed in the same way as the BES data at the other energies [5]. After a cut on the event vertex along the beam direction of ± 70 cm and a cut on the event vertex radial displacement from the mean of 1 cm, there were 17.5 M minimum-bias events available for data analysis. The centrality cuts on "reference multiplicity," which is calculated with all reconstructed particles within $|\eta| < 0.5$ and a distance of closest approach to the primary vertex smaller than 3 cm, were >200 particles for 0–10% centrality, >59 and <200 particles for 10%–40% centrality, and >5 and <59 particles for 40%–80% centrality. The minimum bias results for all three centrality bins combined are shown in Fig. 1. The subevent plane resolution [6] is shown in Fig. 2 compared to other beam energies from previous data sets in the BES. The 14.5 GeV resolution is close to the 11.5 GeV resolution because in 2014 there was additional material between the beam pipe and the time projection chamber (TPC). This caused a lower multiplicity giving a slightly lower resolution than expected based on the other beam energies.

III. CENTRALITY AND ENERGY DEPENDENCE

We present the transverse kinetic energy dependence of v_2 for 0%–10%, 10%–40%, and 40%–80% central Au + Au collisions at $\sqrt{s_{NN}} = 7.7$, 11.5, 14.5, 19.6, 27, 39, and 62.4 GeV. The analysis techniques used for particle identification, event plane reconstruction, and v_2 extraction are the same as the ones previously described [6], and are summarized below.

The identification of charged particles is based on a combination of momentum information, the specific energy loss dE/dx in the time-projection chamber (TPC), and a required time-of-flight measurement with the time-of-flight (ToF) detector. Charged pions and kaons can be easily

distinguished up to 1.0 GeV/c in transverse momentum, whereas at higher momenta the particle species start to significantly overlap. At higher p_{T} two-dimensional Gaussian fits in a combined m^2 vs dE/dx plane were used to statistically extract the particle yield for $\pi^{\pm}$ and $K^{\pm}$ as a function of the relative angle to the reconstructed event plane angle Ψ. For protons only one-dimensional Gaussian fits in m^2 were used to get the yields. The unstable particles K^0_s, ϕ, Λ, Ξ, and Ω, were reconstructed via the invariant mass technique. For weak decay particles, additional topological constraints [6] on the decay kinematics were applied to suppress background. The remaining combinatorial background was subtracted using the mixed event technique.

The event plane was reconstructed using charged particle tracks in the TPC. To suppress nonflow contributions we utilized the η-sub method, with an additional η gap of ± 0.05 between the subevents, and then averaged the results from the two subevents. Recentering, ϕ-weight, and shift techniques were applied for each η hemisphere independently to flatten the event plane [7]. The event plane resolution increases with

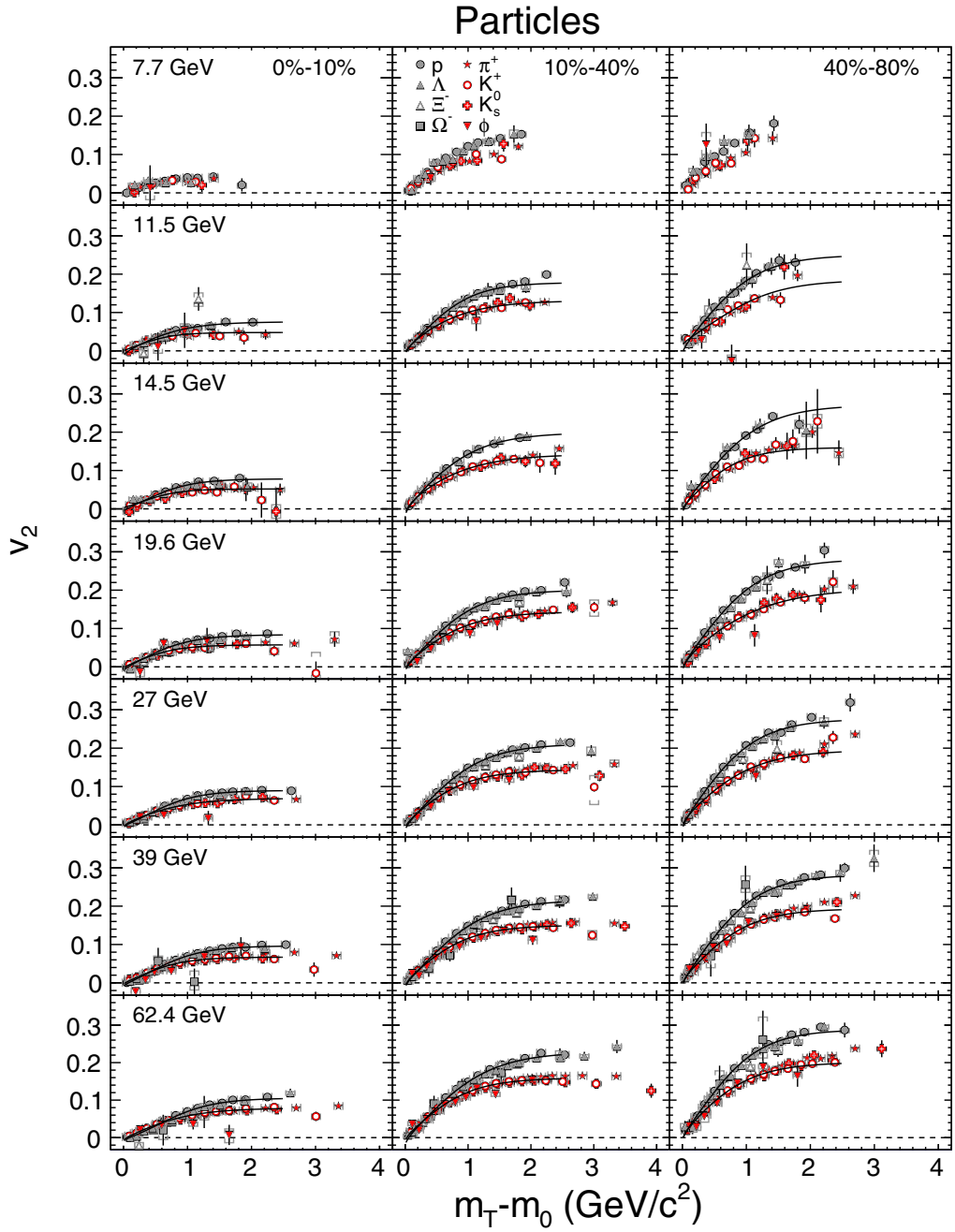

FIG. 3. The elliptic flow v_2 of identified particles (π^+, K^+, K^0_s, p, ϕ, Λ, Ξ^-, Ω^-) as a function of $m_{\mathrm{T}} - m_0$, for 0%–10%, 10%–40%, and 40%–80% central Au + Au collisions at $\sqrt{s_{NN}} = 7.7$, 11.5, 14.5, 19.6, 27, 39, and 62.4 GeV. The lines show simultaneous fits to baryons and mesons with Eq. (1). The systematic errors are shown by the hooked error bars.

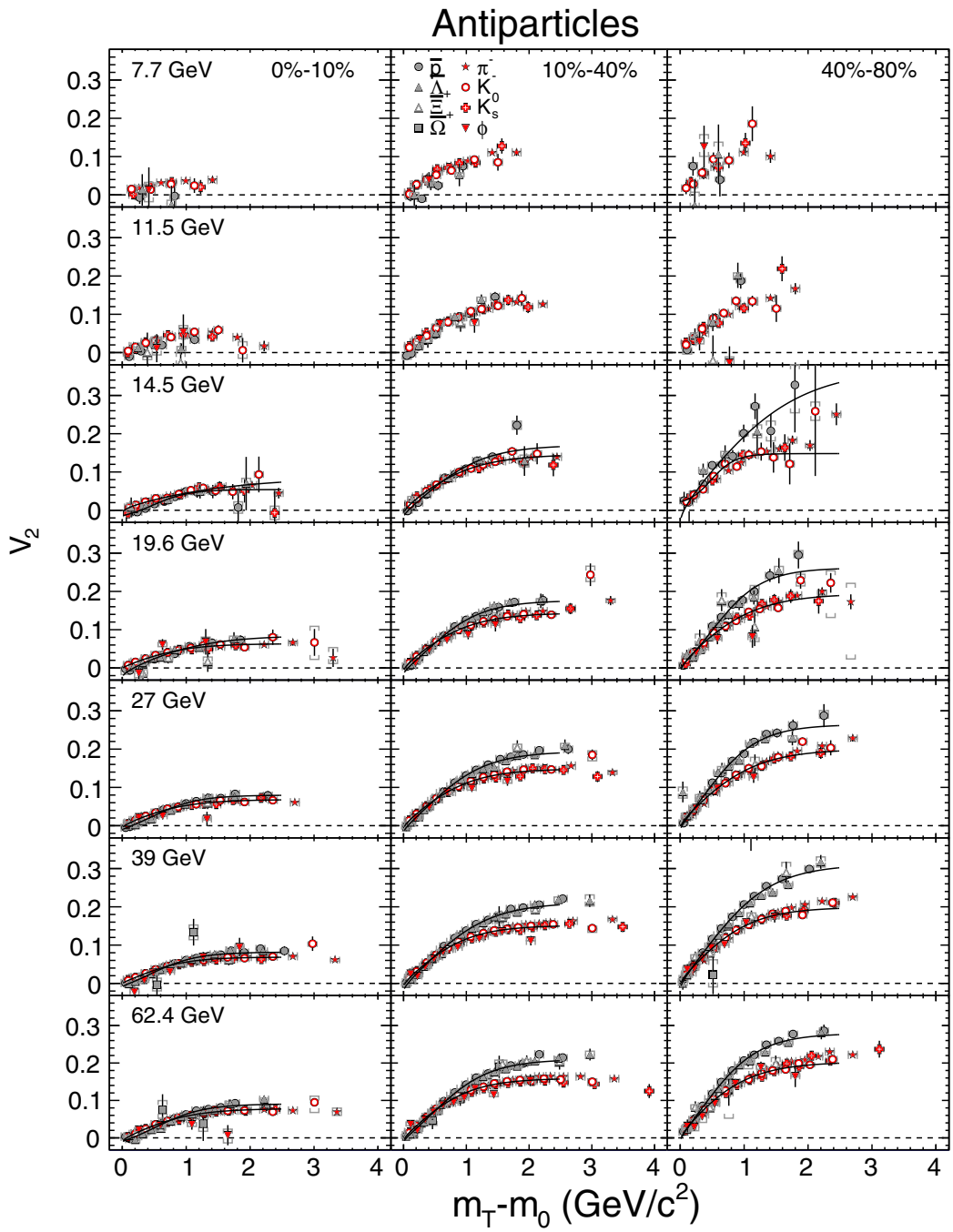

FIG. 4. The elliptic flow v_2 of identified antiparticles (π^-, K^-, K^0_s, $\bar{p}$, ϕ, $\bar{\Lambda}$, $\bar{\Xi}^+$, $\bar{\Omega}^+$) as a function of $m_T - m_0$, for 0%–10%, 10%–40%, and 40%–80% central Au + Au collisions at $\sqrt{s_{NN}} = 7.7$, 11.5, 14.5, 19.6, 27, 39, and 62.4 GeV. The lines show simultaneous fits to baryons and mesons with Eq. (1). The systematic errors are shown by the hooked error bars.

$\sqrt{s_{NN}}$, with maxima as a function of centrality of 35% at $\sqrt{s_{NN}} = 7.7$ GeV and 50% (not shown) at $\sqrt{s_{NN}} = 62.4$ GeV. The systematic errors were estimated as in the previous publication [6].

Figure 3 shows v_2 vs $m_T - m_0$ of particles (π^+, K^+, K^0_s, p, ϕ, Λ, Ξ^-, and Ω^-) for three centrality ranges of Au + Au collisions at $\sqrt{s_{NN}} = 7.7$, 11.5, 14.5, 19.6, 27, 39, and 62.4 GeV. A splitting between baryons and mesons is observed at all energies and centralities except for 7.7 GeV central collisions. Here there are not enough events to allow a conclusion. All the v_2 values increase from central to peripheral collisions.

Figure 4 shows the energy and centrality dependence of v_2 vs. $m_T - m_0$ but for antiparticles (π^-, K^-, K^0_s, $\bar{p}$, ϕ, $\bar{\Lambda}$, $\bar{\Xi}^+$, and $\bar{\Omega}^+$). (K^0_s and ϕ are plotted again since they are their own antiparticles.) The splitting between baryons and mesons is significant at 19.6 GeV and higher energies, and marginally significant at 14.5 GeV. There is no observed splitting for all

centralities at 11.5 GeV and below. For these energies we are limited by the number of events and cannot draw a conclusion. For the ϕ meson at 14.5 GeV there were not enough events to plot the centrality dependence.

In both Figs. 3 and 4, for every particle species, energy, and centrality, v_2 increases with increasing $m_T - m_0$. At $m_T - m_0$ values larger than 1 GeV/c^2 an onset of v_2 saturation can be observed. For the most central 0%–10% collisions the absolute baryon-meson splitting is significantly smaller compared to more peripheral collisions, partly because the values are smaller making the absolute difference smaller.

To quantify the baryon and meson splitting and the scaling with the number of constituent quarks (NCQ), we fit the baryons (B) and mesons (M) separately using the function

$$f_{v_2}(p_T,n) = \frac{an}{1+e^{-(p_T/n-b)/c}} - dn, \qquad (1)$$

where a, b, c, and d are fit parameters and n is the number of constituent quarks in the particle [8]. The ratio $v_2(\mathrm{B})/v_2(\mathrm{M})$ is calculated by the following steps. First, we fit baryons with $n = 3$ and mesons with $n = 2$ using Eq. (1) for particles and for antiparticles. Second, we take the v_2 value from Eq. (1) at $m_T - m_0 = 2$ GeV/c^2 for baryons and at $m_T - m_0 = 2 \times (2/3)$ GeV/c^2 for mesons. That is because we want to compare the corresponding v_2 value after baryons and mesons are scaled by the number of constituent quarks. These p_T values were chosen to be above the hydro region but still where there were data for the lowest beam energy. If there is a perfect NCQ scaling, the ratio $v_2(\mathrm{B})/v_2(\mathrm{M})$ should be equal to 1.5. In Fig. 5, we show this ratio as a function of beam energy for particles and antiparticles in three centrality bins. We can see from Fig. 5 that the baryon-to-meson elliptic flow ratio for particles is higher than for antiparticles at all energies for 0%–10% and 10%–40% central collisions, but has no significant difference between particles and antiparticles for 40%–80%. The ratio for antiparticles shows a centrality dependence which is increasing from central to peripheral from about 1.3 to 1.6. But the ratio for particles does not show a significant centrality dependence. There is no significant beam energy dependence for the ratio of both particles and antiparticles for the points plotted, except for antiparticles at 10%–40% centrality. In addition, we can see from the ratio that NCQ scaling holds for particles at centralities of 0%–10% and 10%–40%, but the ratio is slightly larger at 40%–80%.

In Fig. 6, upper panel, we show the difference in v_2 between particles (π^+, K^+, p, Λ, and Ξ^-) and their corresponding antiparticles (π^-, K^-, $\bar{p}$, $\bar{\Lambda}$, and $\bar{\Xi}^+$) for 10%–40% centrality. The difference is obtained by taking the average ratio in the measured p_T range as was done in Ref. [6]. The 10%–40% results are not very different from those obtained with minimum bias events shown previously [5], but now are shown as a function of centrality in the middle panel for protons and antiprotons. In the lower panel the relative difference normalized by v_2^{norm}, the proton elliptic flow at $p_T = 1.5$ GeV/c, shows a clear centrality dependence with a bigger effect for the more central collisions.

A systematic check has been carried out with the first-harmonic event plane reconstructed by the two beam-beam

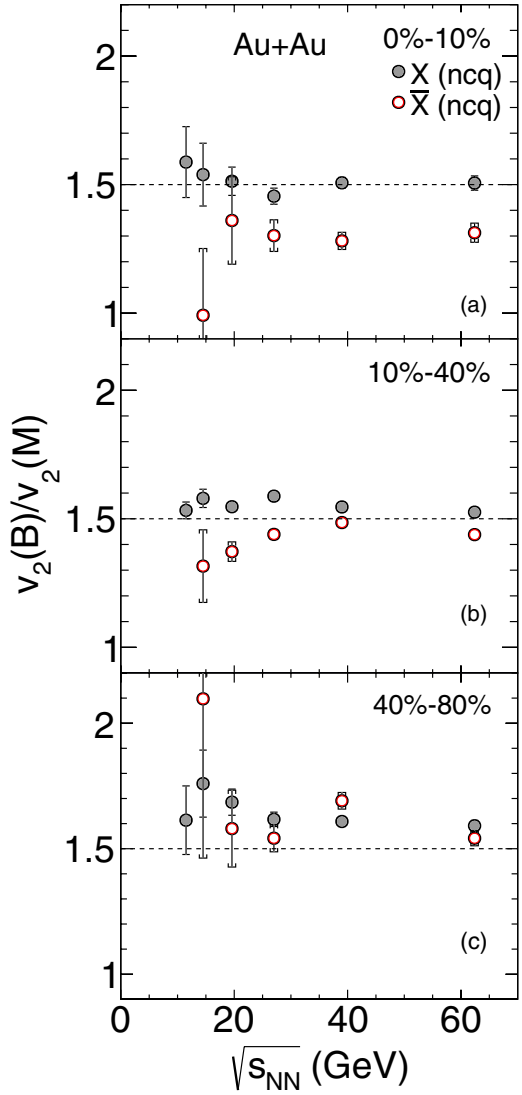

FIG. 5. The ratio of v_2 between baryons (B) and mesons (M) of particles (X) and antiparticles ($\bar{X}$) as a function of $\sqrt{s_{NN}}$ for 0%–10%, 10%–40% and 40%–80% central Au + Au collisions. The values of baryons and mesons are taken from the fit lines in Figs. 3 and 4 with Eq. (1) at the appropriate values of $m_T - m_0$. See text for details. The open points are for antiparticles and the closed points for particles.

counters (BBCs) [9,10] covering $3.3 < |\eta| < 5.0$. The technical details are explained in Ref. [11]. In the η-subevent method for $v_2\{\eta\text{-sub}\}$ there is an η gap of at least 0.3 between the observed event plane and the particles correlated to it in the opposite hemisphere. But using the BBCs this gap is at least 2.0 units of pseudorapidity. Possible systematic uncertainties arise from nonflow, i.e., azimuthal correlations not related to the reaction plane orientation. These nonrelated correlations arise from resonances, jets, quantum statistics, and final-state interactions such as Coulomb effects. They are suppressed by the use of a different harmonic for the event plane and the relatively large pseudorapidity gap between the STAR TPC and the BBC detectors [11,12]. In practice, $v_2\{\mathrm{BBC}\}$ was measured

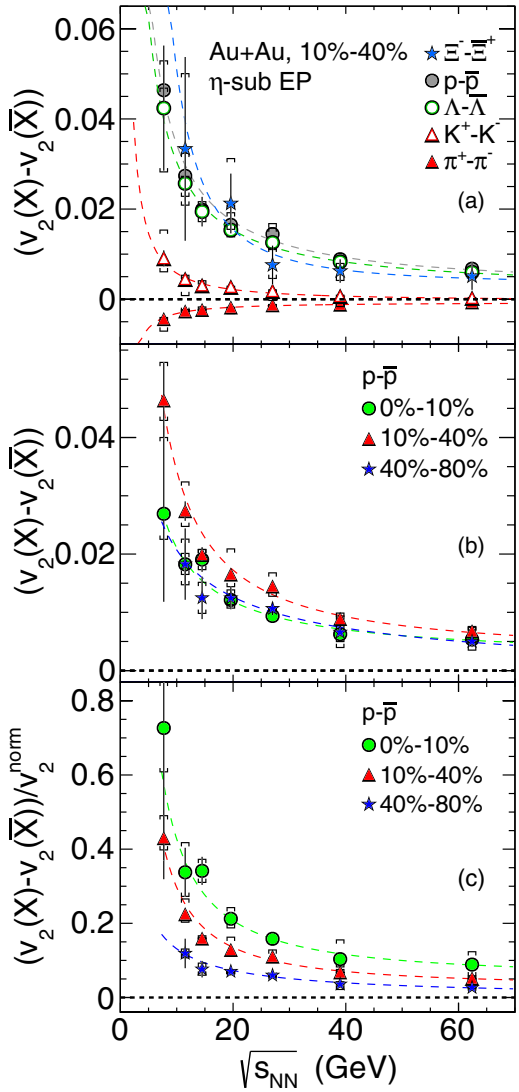

FIG. 6. (a) The difference in v_2 between particles (X) and their corresponding antiparticles ($\bar{X}$) (see legend) as a function of $\sqrt{s_{NN}}$ for 10%–40% central Au + Au collisions. (b) The difference in v_2 between protons and antiprotons as a function of $\sqrt{s_{NN}}$ for 0%–10%, 10%–40% and 40%–80% central Au + Au collisions. (c) The relative difference. The systematic errors are shown by the hooked error bars. The dashed lines in the plot are fits with a power-law function.

in the following way:

$$v_2\{\mathrm{BBC}\} = \langle\cos[2\phi - \Psi_1 - \Psi_2]\rangle / \langle\cos(\Psi_1 - \Psi_2)\rangle, \quad (2)$$

where Ψ_1 and Ψ_2 are the first-harmonic subevent planes from the two BBC detectors.

The use of the first-harmonic event plane also reduces the event-by-event flow fluctuation contribution compared with the $v_2\{\eta\text{-sub}\}$ method in which the second-harmonic event plane was used to calculate the second-harmonic anisotropy. Figure 7 presents a comparison between $v_2\{\mathrm{BBC}\}$ and $v_2\{\eta\text{-sub}\}$, in terms of the v_2 difference between protons and antiprotons (and between π^+ and π^-). We focus on the center-of-mass energies below 20 GeV where the v_2 difference between particles and antiparticles is most pronounced. For

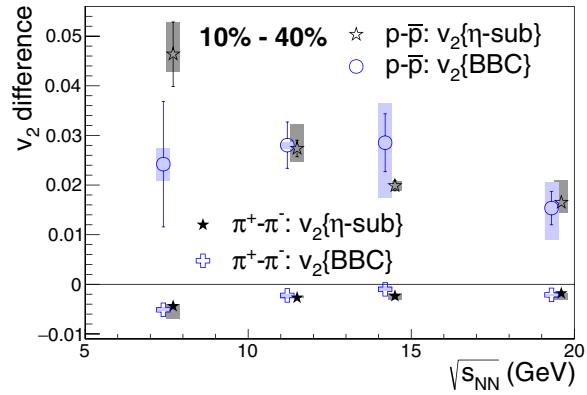

FIG. 7. The v_2 difference between protons and antiprotons (and between π^+ and π^-) for 10%–40% centrality Au+Au collisions at 7.7, 11.5, 14.5, and 19.6 GeV. The $v_2\{\mathrm{BBC}\}$ results were slightly shifted horizontally.

10%–40% most central Au + Au collisions at 7.7, 11.5, 14.5, and 19.6 GeV, the results from the two methods are consistent with each other within the already quoted uncertainties. This indicates that the v_2 difference is a robust observable and is not dominated by nonflow or flow fluctuations.

IV. AMPT

Calculations using AMPT were performed [13]. The AMPT model is a transport model with four main components: the initial conditions, partonic interactions, conversion from the partonic to hadronic matter, and hadronic interactions [14]. It has two different versions to deal with different scenarios: the default AMPT model and the string melting AMPT model. The initial conditions are generated by the HIJING (heavy ion jet interaction generator) model [15–17]. The HIJING model includes only two-body nucleon-nucleon

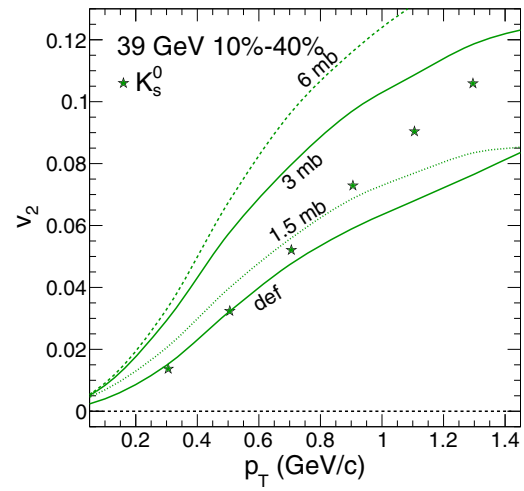

FIG. 8. Elliptic flow v_2 as a function of p_T for K^0_s data at $\sqrt{s_{NN}} = 39$ GeV for 10%–40% centrality. The curves are for AMPT default and AMPT string melting with cross sections of 1.5, 3.0, and 6.0 mb.

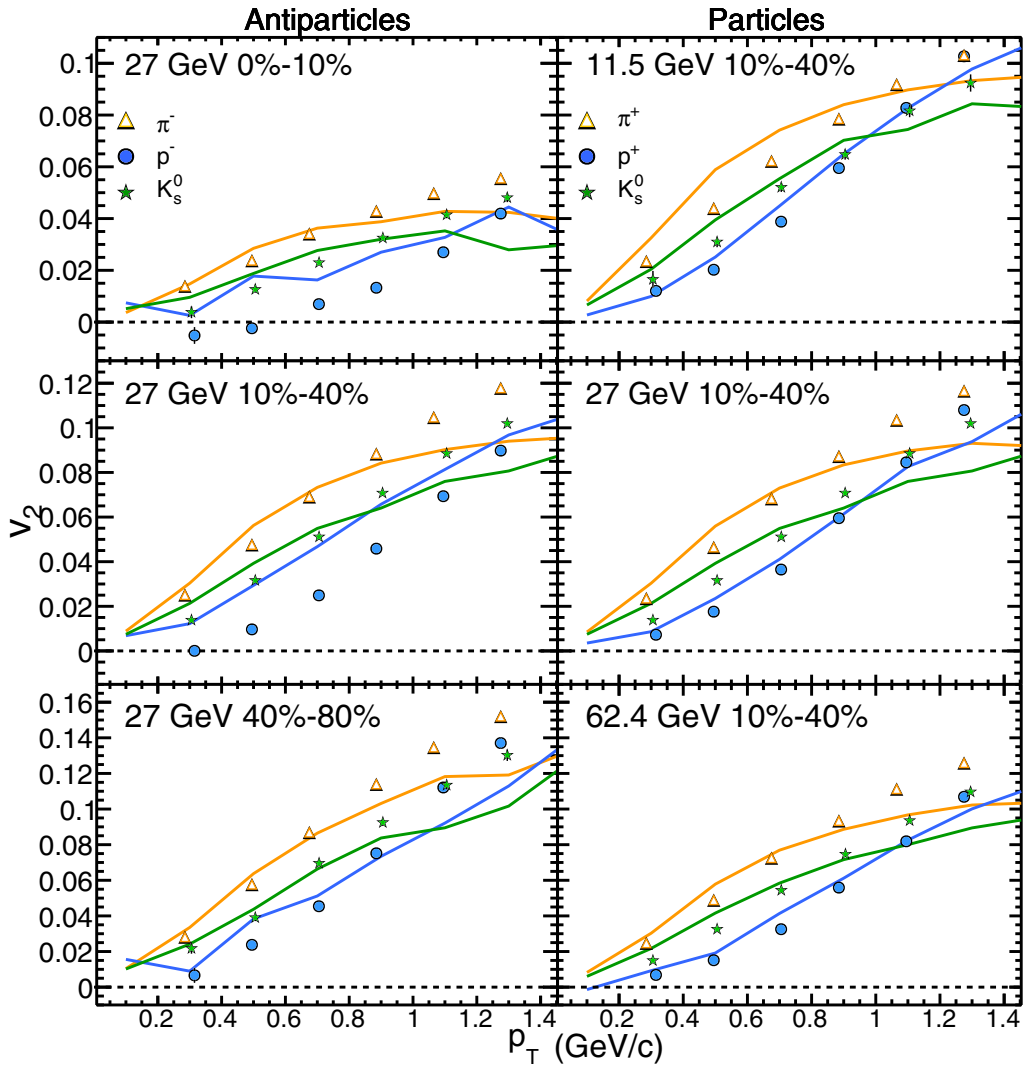

FIG. 9. Elliptic flow v_2 as a function of p_T for particles and antiparticles. The symbols show the experimental data. The error bars are mostly smaller than the points. The lines, with the same color code and the same order, show the AMPT string melting calculations with a cross section 1.5 mb. Antiparticles are on the left for three centrality bins. Particles are on the right for three beam energies.

interactions and generates minijets and excited strings through hard processes and soft processes separately. Excited strings are treated differently in the default and string melting models. In the default model, excited strings combine to form hadrons according to the Lund string fragmentation model, which then go through a hadronic interaction stage. In the string melting model, excited strings first convert to partons (melting) then have partonic interactions with the original soft partons. The partonic interactions for both the default and string melting models are described by the ZPC (Zhang's parton cascade) model [18]. In the final stage of the ZPC model, partons in the default model recombine with parent strings and hadronize through the Lund string fragmentation model. However, in the string melting model, the hadronization of partons is described by a coalescence model. In both models after hadronization, the hadronic interactions are modeled by the ART (a relativistic transport) model [19,20].

Approximately 10 to 20 million events were generated for each case for 0%–80% central Au+Au collisions at $\sqrt{s_{NN}} =$ 11.5, 27, 39, and 62.4 GeV with the default model (v1.25) and the string melting model (v2.25) with three different parton scattering cross sections (1.5, 3, and 6 mb). The same η-subevent method was used to calculate elliptic flow. Figure 8 shows K^0_s data compared to $\sqrt{s_{NN}} = 39$ GeV AMPT default and AMPT string melting with cross sections of 1.5, 3.0, and 6.0 mb. Although the shapes are not the same, the 1.5 mb curve seems to be the best compromise (see also Ref. [13]). The curves with larger cross sections are all above the data points with deviations on the order of a factor 2 at $p_T < 2$ GeV/c. Figure 9 shows comparisons of data with the AMPT string melting calculations with a cross section of 1.5 mb. The larger values of v_2 for protons compared to antiprotons can be seen in the middle panels for 27 GeV 10%–40%. Basic features of the data, such as mass

ordering and baryon-meson crossing at intermediate p_T, are well reproduced by AMPT. The calculations are furthermore in a reasonable quantitative agreement with the data for K_s^0 and protons, but deviate significantly for antiprotons in central and mid-central collisions. This shows that the particle-antiparticle difference, at least for protons, is not reproduced by AMPT. The pion v_2 is similar at low p_T but systematically deviates to smaller values from the data at transverse momenta larger than 1 GeV/c.

Figure 10 shows the v_2 difference for protons minus antiprotons for $\sqrt{s_{NN}} = 27$ GeV. It seems that there is little difference predicted by the AMPT calculations. AMPT does not explain the effect seen in the data. It was pointed out [6] that by including mean-field potentials [21] in the hadronic phase of the AMPT model, the difference in elliptic flow between protons and antiprotons can be qualitatively reproduced, but then the charged kaon difference can not be reproduced.

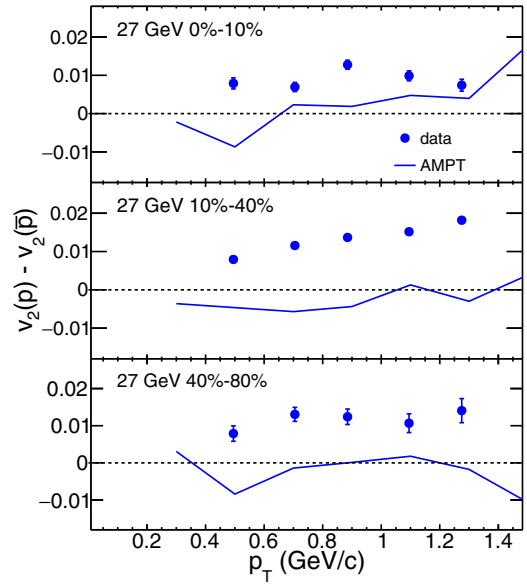

FIG. 10. Elliptic flow v_2 as a function of p_T for protons minus antiprotons at $\sqrt{s_{NN}} = 27$ GeV for three centralities. The curves are for AMPT string melting with cross sections of 1.5 mb. The symbols are data.

V. BLAST WAVE FITS

In order to understand the hydrodynamic behavior of $v_2(p_T)$ and its dependence on hadron mass and radial flow, we have applied a version of the "blast wave" model [22] which has four fit parameters: kinetic freeze-out temperature (T), transverse expansion rapidity (ρ_0), the momentum space variation in the azimuthal density (ρ_a), and the coordinate space variation in the azimuthal density (s_2). The blast wave equation we use is [23]

$$v_2(p_T) = \frac{\int_0^{2\pi} d\phi_s \cos(2\phi_s) I_2[\alpha_t(\phi_s)] K_1[\beta_t(\phi_s)][1 + 2s_2 \cos(2\phi_s)]}{\int_0^{2\pi} d\phi_s I_0[\alpha_t(\phi_s)] K_1[\beta_t(\phi_s)][1 + 2s_2 \cos(2\phi_s)]}. \quad (3)$$

The I_0, I_2, and K_1 are modified Bessel functions, where $\alpha_t(\phi_s) = (p_T/T)\sinh[\rho(\phi_s)]$ and $\beta_t(\phi_s) = (m_T/T)\cosh[\rho(\phi_s)]$. The basic assumptions of this blast wave model are boost-invariant longitudinal expansion [24] and freeze-out at constant temperature T on a thin shell [25], which expands with a transverse rapidity exhibiting a second harmonic azimuthal modulation given by $\rho(\phi_s) = \rho_0 + \rho_a \cos 2\phi_s$ [22]. In this equation, ϕ_s is the azimuthal angle in coordinate space; ρ_0 and ρ_a are respectively the transverse

TABLE I. Fit parameters ρ_0, ρ_a, and s_2 for the particle group (X) and the antiparticle group ($\bar{X}$) from Au + Au collisions at $\sqrt{s_{NN}} =$ 7.7–62.4 GeV for three centralities.

Centrality	Parameter	7.7 GeV	11.5 GeV	14.5 GeV	19.6 GeV	27 GeV	39 GeV	62.4 GeV
0%–10%	$\rho_0(X)$		0.51 ± 0.05	0.50 ± 0.02	0.51 ± 0.01	0.55 ± 0.01	0.57 ± 0.01	0.62 ± 0.01
	$\rho_0(\bar{X})$		0.96 ± 0.12	1.16 ± 0.13	0.87 ± 0.04	0.78 ± 0.02	0.76 ± 0.01	0.69 ± 0.02
	$\rho_a(\times 10^{-2}\ X)$		2.24 ± 0.26	2.36 ± 0.09	2.56 ± 0.05	2.46 ± 0.08	2.79 ± 0.06	2.97 ± 0.04
	$\rho_a(\times 10^{-2}\ \bar{X})$		2.14 ± 0.28	1.54 ± 0.26	2.07 ± 0.13	2.46 ± 0.09	2.40 ± 0.06	2.98 ± 0.08
	$s_2(\times 10^{-2}\ X)$		0.03 ± 3.37	0.00 ± 1.10	0.00 ± 0.60	0.52 ± 0.18	0.12 ± 0.14	0.00 ± 0.64
	$s_2(\times 10^{-2}\ \bar{X})$		2.09 ± 0.57	2.32 ± 0.35	1.81 ± 0.22	1.31 ± 0.17	1.53 ± 0.10	0.37 ± 0.19
10%–40%	$\rho_0(X)$	0.38 ± 0.03	0.42 ± 0.01	0.44 ± 0.01	0.46 ± 0.01	0.48 ± 0.00	0.50 ± 0.00	0.53 ± 0.00
	$\rho_0(\bar{X})$	1.08 ± 0.10	0.79 ± 0.03	0.67 ± 0.02	0.64 ± 0.01	0.61 ± 0.01	0.59 ± 0.00	0.59 ± 0.01
	$\rho_a(\times 10^{-2}\ X)$	4.39 ± 0.28	4.41 ± 0.14	4.55 ± 0.15	4.47 ± 0.08	4.55 ± 0.05	4.75 ± 0.04	5.19 ± 0.05
	$\rho_a(\times 10^{-2}\ \bar{X})$	3.47 ± 0.36	4.22 ± 0.18	4.48 ± 0.17	4.62 ± 0.08	4.80 ± 0.05	5.05 ± 0.04	5.24 ± 0.05
	$s_2(\times 10^{-2}\ X)$	1.56 ± 0.72	2.66 ± 0.31	2.64 ± 0.33	2.94 ± 0.16	2.93 ± 0.11	2.82 ± 0.08	2.45 ± 0.10
	$s_2(\times 10^{-2}\ \bar{X})$	5.02 ± 0.70	3.87 ± 0.33	3.19 ± 0.32	3.03 ± 0.16	2.81 ± 0.11	2.67 ± 0.08	2.71 ± 0.10
40%–80%	$\rho_0(X)$		0.33 ± 0.04	0.33 ± 0.03	0.33 ± 0.02	0.37 ± 0.01	0.39 ± 0.01	0.41 ± 0.01
	$\rho_0(\bar{X})$		0.63 ± 0.09	0.41 ± 0.06	0.51 ± 0.03	0.47 ± 0.02	0.48 ± 0.01	0.47 ± 0.01
	$\rho_a(\times 10^{-2}\ X)$		5.15 ± 0.75	5.93 ± 0.67	4.85 ± 0.41	5.13 ± 0.22	4.96 ± 0.14	5.58 ± 0.17
	$\rho_a(\times 10^{-2}\ \bar{X})$		4.69 ± 0.79	7.09 ± 0.28	5.90 ± 0.39	5.75 ± 0.23	5.77 ± 0.14	5.92 ± 0.17
	$s_2(\times 10^{-2}\ X)$		5.60 ± 2.20	3.87 ± 1.87	7.66 ± 1.30	6.91 ± 0.59	7.35 ± 0.35	6.39 ± 0.39
	$s_2(\times 10^{-2}\ \bar{X})$		4.93 ± 1.22	0.00 ± 1.52	3.29 ± 0.79	3.83 ± 0.48	4.79 ± 0.27	5.31 ± 0.34

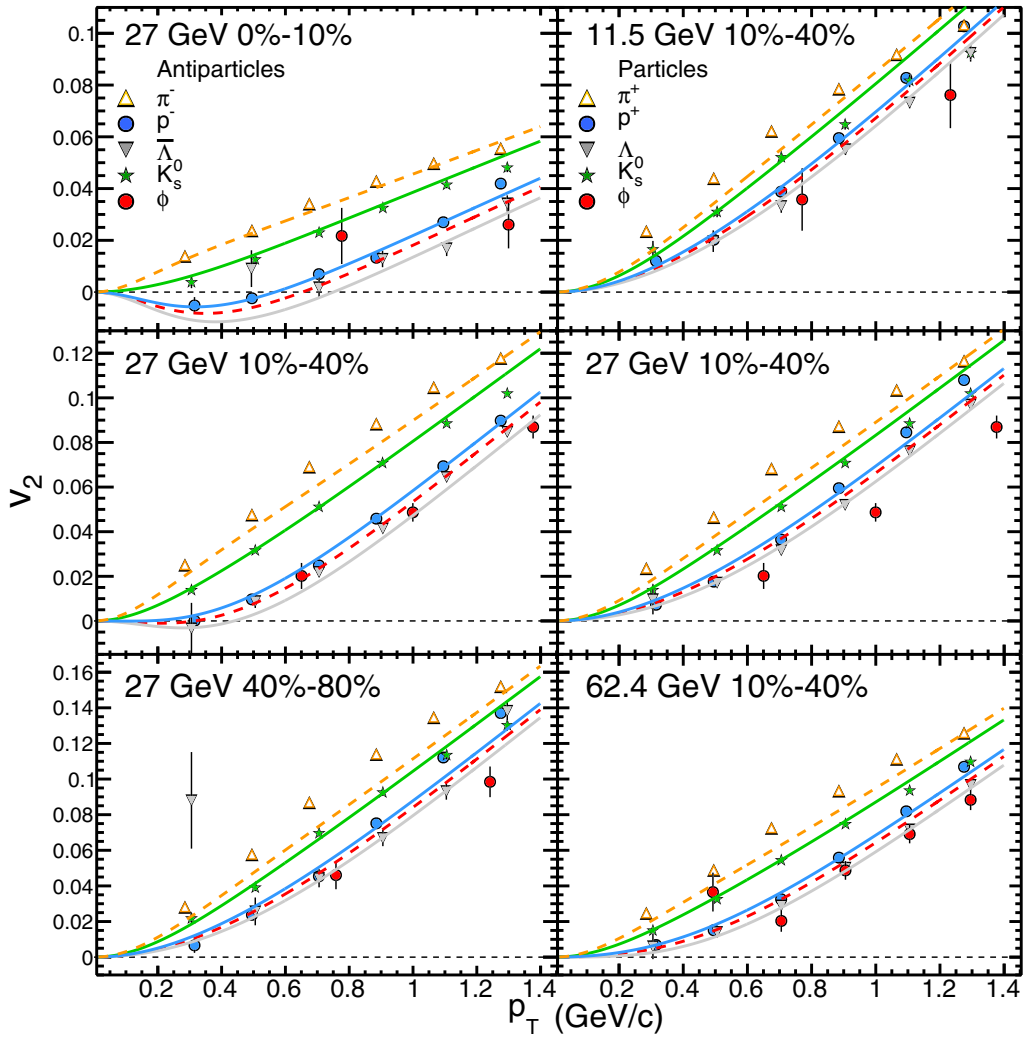

FIG. 11. Elliptic flow v_2 as a function of p_T for particles and antiparticles. The data are shown by symbols. On the left side are blast wave fits (lines) for three centrality bins for $\sqrt{s_{NN}} = 27$ GeV. On the right side are blast wave fits for three beam energies for 10%–40% centrality. Antiparticles are on the left, particles on the right. The lines are the same color and in the same order as the points. The dashed lines for π and ϕ are not fits, but predictions based on the other fits. The error bars depict the combined statistical and systematic errors.

expansion rapidity and the amplitude of its azimuthal variation. Secondly, $\beta = \tanh(\rho_0)$, where β is the transverse expansion velocity which is the velocity of the radial flow. Finally, $\beta_a = \tanh^{-1}(\rho_a)$, where β_a is the transverse expansion velocity second harmonic variation which is related to v_2. It needs to be noticed that the mass for different particle species enters in m_T in $\beta_t(\phi_s)$ only. When we do the simultaneous fits, which will be explained below, the only difference between the fits to different particle species is their mass.

We do blast wave fits for $v_2(p_T)$ for each centrality in the following way. First, we apply a cut on $m_T - m_0 < 0.9$ GeV to avoid the nonhydro region at high p_T. Second, the fits for particles (K^+, K^0_s, p, and Λ) and antiparticles (K^-, K^0_s, $\bar{p}$, and $\bar{\Lambda}$) are separated, since we know that they have different behavior [2]. The K^0_s and ϕ meson are plotted as both particles and antiparticles, since the antiparticles for K^0_s and ϕ mesons are themselves. Third, pions are excluded from the fits since many pions come from feed-down from resonance decays [26]. This causes them not to have the proper shape for a blast wave equation fit. Also, ϕ mesons are not included in the fits because of their large error bars. Fourth, the fits are simultaneous fits which means that we use $v_2(p_T)$ of all of the species of particles or antiparticles to minimize the χ^2 of the fit. We do not have spectra for most of the energies and therefore cannot use spectra to constrain the temperature. Instead we input a temperature in a reasonable range [27]. In this paper we choose $T = 120$ MeV as the input, but will show also the results for 100 and 140 MeV.

In Fig. 11, we show examples of the centrality and energy dependence of simultaneous blast wave fits for K^0_s, p, and Λ. The fits are done separately for particles and antiparticles. The dashed lines for π and ϕ are not fits, but predictions based on the other fits. In the left side, we show the simultaneous blast wave fits for various centralities for antiparticles at 27 GeV. We can see the splitting of different particle species is decreasing when we go from central to peripheral, which indicates the decreasing radial flow for antiparticles. On the right, we show the simultaneous blast wave fits for 10%–40%

centrality at 11.5, 27, and 62.4 GeV for particles. We can see the splitting is slightly increasing with increasing energy, which indicates the increasing radial flow with increasing beam energy. If we compare the middle panel from the left and right sides, 10%–40% at 27 GeV for particles and antiparticles, we can see the splitting of antiparticles is larger than that of particles, which suggests the radial flow for antiparticles is larger than for particles. The pion predictions are somewhat low compared to data because the predictions do not include pions from resonance decay [28]. It is worth noting that the v_2 values of the ϕ meson are plotted at the same position for particles and antiparticles, but the predictions from the blast wave model (lower dashed lines in Fig. 11) are different. The fits are different because they are dominated by protons and antiprotons, which are different. For most of the panels the agreement with the data is better with these fits. The v_2 values of K^0_s are the same in both columns, and the v_2 of K^+ and K^- (which are not shown here) are similar.

Although only examples of the fits are shown in Fig. 11, all the fit parameters are shown in Table I. At the lowest beam energy there were only enough data to fit the 10%–40% centrality. The goodness of fits were comparable to those reported in Ref. [23]. Without feed-down correction the χ^2/ndf values are only close to 1 at the lower energies, where the statistical errors are of the order of the expected feed down effects. At higher energies the error bars are much smaller. The resulting χ^2/ndf values rise up to a maximum of 35 for the particle group at $\sqrt{s_{NN}} = 39$ GeV, whereas they are below 1.5 for all energies when feed-down contributions [23] are included in the error bars. For antiparticles the χ^2/ndf values are systematically lower compared to the particle group, with a maximum of 17, while they are about 1.5 with estimated feed-down contributions taken into account.

In Fig. 12, we show the transverse radial velocity parameter, which is extracted from the blast wave fits, as a function of beam energy for three centralities. We can see that at all three centralities the radial flow velocities for antiparticles are larger than for particles, and the difference in β is generally increasing with decreasing energy. This was already seen for minimum bias collisions [23], but now we also see it as a function of centrality. A large transverse radial velocity means that the $v_2(p_T)$ values are smaller because they are spread over a larger p_T range. The decrease in the difference between particles and antiparticles with increasing beam energy, suggests the radial flow velocities are becoming similar. Equal radial velocities have been observed at a beam energy of 200 GeV [23]. We can see that the mean value of radial velocity for both particles and antiparticles is decreasing when we go from central to peripheral, which we have already seen from Fig. 11. Another thing we have already seen from Fig. 11 is that the radial flow velocity is increasing with increasing beam energy for particles. To check if these trends are an artifact of the multiparameter fitting procedure, we have fixed the s_2 parameter at 0.02 as shown in Fig. 12. It makes little difference for 10%–40% and 40%–80% centrality. However, for central collisions β is larger with a smaller gap between particles and antiparticles.

It is surprising to see a generally decreasing trend in β for antiparticles with increasing beam energy. We can speculate

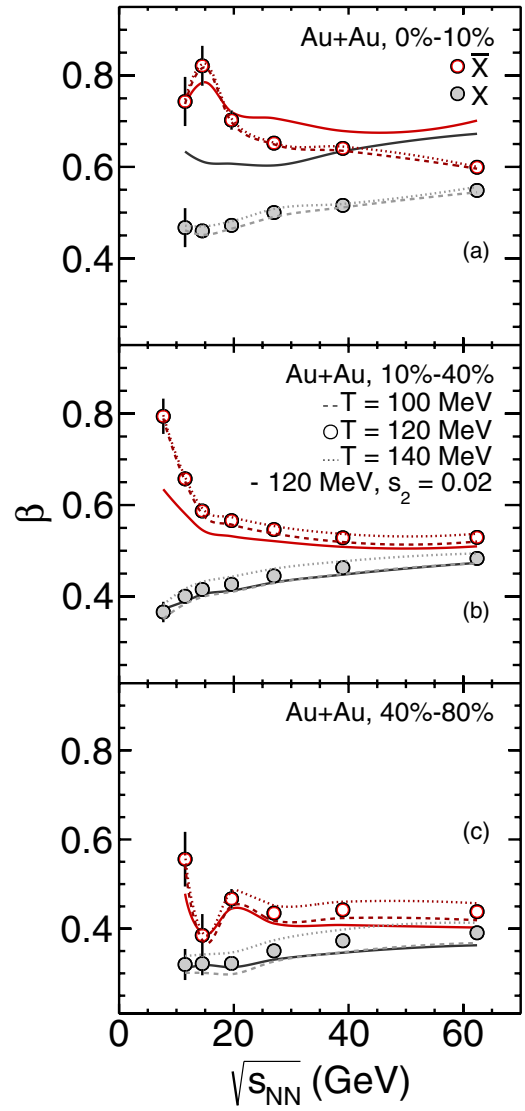

FIG. 12. The transverse radial velocity parameter β as a function of $\sqrt{s_{NN}}$ for Au + Au collisions for three centralities and three assumed temperatures. The circles are for 120 MeV, open red circles for antiparticles, and closed black circles for particles. The error bars seen at low beam energies depict the combined statistical and systematic errors. The solid red and black lines show the result when the s_2 parameter is fixed at 0.02 and the temperature held at 120 MeV.

[23] that at lower beam energy the antiparticles can only be produced at early time or not produced at all. Therefore, the produced antiparticles go through the whole expansion stage and get larger transverse expansion velocity than the particles which can be produced or transported in the latter stage. In addition, at lower collision energies, the absorption becomes important, especially for antibaryons. This effect also will lead to a higher value of mean p_T or, in the language of the blast wave fit, to a larger value of β. At higher beam energy, the antiparticles can be also produced in the latter stage of the evolution, and then only go through part of the expansion and get smaller transverse expansion velocity. At 14.5 GeV the bump for central collisions and the dip for peripheral collisions

are probably statistical fluctuations plus some correlations with other parameters.

VI. SUMMARY

For 14 identified particles (π^-, π^+, K^-, K^+, K^0_s, p, $\bar{p}$, ϕ, Λ, $\bar{\Lambda}$, Ξ^-, $\bar{\Xi}^+$, Ω^-, and $\bar{\Omega}^+$), we have measured the elliptic flow v_2 for Au + Au collisions for seven beam energies ($\sqrt{s_{NN}}$ = 7.7, 11.5, 14.5, 19.6, 27, 39, and 62.4 GeV), and three centralities (0%–10%, 10%–40%, and 40%–80%). The baryon-meson splitting at intermediate p_T is in reasonable agreement with NCQ scaling for all energies and centralities reported here. The v_2 of baryons is larger than for antibaryons for all beam energies, and the relative increase for protons compared to antiprotons [see Fig. 6 (c)] is larger for central collisions.

AMPT calculations with string melting with a 1.5 mb partonic cross section do not explain the proton-antiproton difference.

With a blast wave model we have fit the results for particles (K^+, K^0_s, p, Λ) and antiparticles (K^-, K^0_s, $\bar{p}$, $\bar{\Lambda}$) separately with three blast wave parameters (ρ_0, ρ_a, and s_2). The significant parameter which changes the most with beam energy is the transverse radial velocity (β) which comes from ρ_0. Its value is much larger for antiparticles than particles, but the difference decreases with increasing beam energy. It is also larger for central collisions than peripheral collisions. The behavior of this transverse radial flow parameter quantifies the v_2 particle-antiparticle difference observed above and published previously for minimum bias collisions [2].

ACKNOWLEDGMENTS

We thank the RHIC Operations Group and RCF at BNL, the NERSC Center at LBNL, the KISTI Center in Korea, and the Open Science Grid consortium for providing resources and support. This work was supported in part by the Office of Nuclear Physics within the U.S. DOE Office of Science, the U.S. NSF, the Ministry of Education and Science of the Russian Federation, NNSFC, CAS, MoST and MoE of China, the National Research Foundation of Korea, GA and MSMT of the Czech Republic, FIAS of Germany, DAE, DST, and UGC of India, the National Science Centre of Poland, National Research Foundation, the Ministry of Science, Education and Sports of the Republic of Croatia, and RosAtom of Russia.

[1] M. M. Aggarwal *et al.* (STAR Collaboration), An Experimental exploration of the QCD phase diagram: The search for the critical point and the onset of de-confinement, arXiv:1007.2613.

[2] L. Adamczyk *et al.* (STAR Collaboration), Observation of an Energy-Dependent Difference in Elliptic Flow between Particles and Antiparticles in Relativistic Heavy Ion Collisions, Phys. Rev. Lett. **110**, 142301 (2013).

[3] Y. B. Ivanov and A. A. Soldatov, Elliptic flow in heavy-ion collisions at energies $\sqrt{s_{NN}}$ = 2.7–39 GeV, Phys. Rev. C **91**, 024914 (2015).

[4] Y. Hatta, A. Monnai, and B.-W. Xiao, Flow harmonics v_n at finite density, Phys. Rev. D **92**, 114010 (2015).

[5] L. Adamczyk *et al.* (STAR Collaboration), Inclusive charged hadron elliptic flow in Au + Au collisions at $\sqrt{s_{NN}}$ = 7.7–39 GeV, Phys. Rev. C **86**, 054908 (2012).

[6] L. Adamczyk *et al.* (STAR Collaboration), Elliptic flow of identified hadrons in Au + Au collisions at $\sqrt{s_{NN}}$ = 7.7–62.4 GeV, Phys. Rev. C **88**, 014902 (2013).

[7] S. A. Voloshin, A. M. Poskanzer, and R. Snellings, Collective phenomena in non-central nuclear collisions, in *Relativistic Heavy Ion Physics*, Landolt-Börnstein, Group 1, Vol. 23 (Springer-Verlag, Berlin, 2010), pp. 5–54; arXiv:0809.2949.

[8] X. Dong, S. Esumi, P. Sorensen, N. Xu, and Z. Xu, Resonance decay effects on anisotropy parameters, Phys. Lett. B **597**, 328 (2004).

[9] C. A. Whitten (STAR Collaboration), The beam-beam counter: A local polarimeter at STAR, in *Polarized Ion Sources, Targets and Polarimetry - PSTP2007: 12th International Workshop*, September 2007, Upton, NY, edited by E. Kponou, Y. Makdisi, and A Zelenski, AIP Conf. Proc. No. 980 (AIP, New York, 2008), p. 390.

[10] F. S. Bieser *et al.*, The STAR trigger, Nucl. Instrum. Methods A **499**, 766 (2003).

[11] G. Agakishiev *et al.* (STAR Collaboration), Directed and elliptic flow of charged particles in Cu + Cu collisions at $\sqrt{s_{NN}}$ = 22.4 GeV, Phys. Rev. C **85**, 014901 (2012).

[12] A. M. Poskanzer and S. A. Voloshin, Methods for analyzing anisotropic flow in relativistic nuclear collisions, Phys. Rev. C **58**, 1671 (1998).

[13] X. Sun, J. Liu, A. Schmah, S. Shi, J. Zhang, L. Huo and H. Jiang, Elliptic and triangular flow of identified particles from the AMPT model at RHIC energies, J. Phys. G **42**, 115101 (2015).

[14] Z. W. Lin, C. M. Ko, B. A. Li, B. Zhang, and S. Pal, A Multi-phase transport model for relativistic heavy ion collisions, Phys. Rev. C **72**, 064901 (2005).

[15] M. Gyulassy and X. N. Wang, HIJING 1.0: A Monte Carlo program for parton and particle production in high-energy hadronic and nuclear collisions, Comput. Phys. Commun. **83**, 307 (1994).

[16] X. N. Wang, Role of multiple mini-jets in high-energy hadronic reactions, Phys. Rev. D **43**, 104 (1991).

[17] X. N. Wang and M. Gyulassy, HIJING: A Monte Carlo model for multiple jet production in p-p, p-A and A-A collisions, Phys. Rev. D **44**, 3501 (1991).

[18] B. Zhang, ZPC 1.0.1: A Parton cascade for ultrarelativistic heavy ion collisions, Comput. Phys. Commun. **109**, 193 (1998).

[19] B. A. Li and W. Bauer, Pion spectra in a hadronic transport model for relativistic heavy ion collisions, Phys. Rev. C **44**, 450 (1991).

[20] B. A. Li and C. M. Ko, Formation of superdense hadronic matter in high-energy heavy ion collisions, Phys. Rev. C **52**, 2037 (1995).

[21] J. Xu, L. W. Chen, C. M. Ko, and Z. W. Lin, Effects of hadronic potentials on elliptic flows in relativistic heavy ion collisions, Phys. Rev. C **85**, 041901 (2012).

[22] C. Adler *et al.* (STAR Collaboration), Identified particle elliptic flow in Au + Au collisions at $\sqrt{s_{NN}} = 130$ GeV, Phys. Rev. Lett. **87**, 182301 (2001).

[23] X. Sun, H. Masui, A. M. Poskanzer, and A. Schmah, Blast wave fits to elliptic flow data at $\sqrt{s_{NN}} = 7.7$–2760 GeV, Phys. Rev. C **91**, 024903 (2015).

[24] J. D. Bjorken, Highly relativistic nucleus-nucleus collisions: The central rapidity region, Phys. Rev. D **27**, 140 (1983).

[25] F. Cooper and G. Frye, Comment on the single particle distribution in the hydrodynamic and statistical thermodynamic models of multiparticle production, Phys. Rev. D **10**, 186 (1974).

[26] G. E. Brown, J. Stachel and G. M. Welke, Pions from resonance decay in Brookhaven relativistic heavy ion collisions, Phys. Lett. B **253**, 19 (1991).

[27] M. von Leeuwan (NA49 Collaboration), Recent results on spectra and yields from NA49, Nucl. Phys. A **715**, 161c (2003).

[28] V. Greco and C. M. Ko, Effect of resonance decays on hadron elliptic flows, Phys. Rev. C **70**, 024901 (2004).